Int J Adv Manuf Technol (2013) 64:1587–1597
DOI 10.1007/s00170-012-4125-0

ORIGINAL ARTICLE

A reliable method for predicting serrated chip formation in high-speed cutting: analysis and experimental verification

Chunzheng Duan · Liangchi Zhang

Received: 18 September 2011 / Accepted: 29 March 2012 / Published online: 5 May 2012

Abstract Serrated chip formation influences almost every aspect of a high-speed cutting (HSC) process. This paper aims to develop a reliable method to accurately predict such chip formation processes. To this end, a systematic finite element analysis was carried out and a series of HSC experiments were conducted on a heat treated AISI 1045 steel. It was found that the integrative use of the Johnson–Cook thermal-viscoplastic constitutive equation, Johnson–Cook damage criterion for chip separation, and the modified Zorev's friction model can precisely predict the serrated chip formation in HSC without artificial assumptions. This advancement has removed the major barrier in the current machining investigations by numerical simulation. The present study also found that the tool rake angle has a significant effect on serrated chip formation. As the rake angle increases, the chip sawtooth degree and cutting forces decrease, but the chip segmentation frequency increases.

Keywords High-speed cutting (HSC) · Finite element simulation · Serrated chip · Chip separation criterion · Friction

C. Duan · L. Zhang (✉)
School of Mechanical and Manufacturing Engineering,
University of New South Wales,
NSW, 2052 Sydney, Australia
e-mail: liangchi.zhang@unsw.edu.au

C. Duan
School of Mechanical Engineering,
Dalian University of Technology,
116024 Dalian, People's Republic of China

1 Introduction

High-speed cutting (HSC) has been widely used in aeronautics and astronautics, automobile, mould, and optical engineering, due to its high production efficiency and much improved product quality. Nevertheless, the full control of HSC requires a precise understanding of the dependence of material deformation and removal mechanisms on the complex coupling of high strain rate, high strain and high temperature rise. For instance, a most evident difference between an HSC and a conventional cutting is that the former produces serrated chips (also referred to as segmented or saw-toothed chips). Many studies reported that it was the formation of the serrated chips that influenced almost every aspect of the HSC, such as the cutting forces, cutting temperature, tool wear, and product quality of a machined component. Therefore, it has become necessary to understand the mechanisms of serrated chip formation, the effect of chip geometry on cutting forces, and their relations with the properties of a workpiece material and cutting conditions.

Over the past decade, investigations on serrated chip formation have been mostly associated with theoretical modeling and finite element (FE) simulations. For example, Klocke et al. [1] conducted an FE simulation of the orthogonal HSC of AISI 1045 with the aid of a commercial FE code DEFORM 2D. In the simulation, they used a thermal elastic–plastic constitutive equation and assumed that the friction across the chip–tool interface was a constant (friction coefficient=0.2). Their criterion to deal with the chip separation was not clearly given. Baker et al. [2] and Baker [3] simulated the serrated chip formation in HSC and the forces when cutting Ti6Al4V alloy with adiabatic shear, using ABAQUS. Their simulation applied a generic flow stress law with strain hardening, thermal softening, and rate-dependent hardening based on the flow stress measurements

by the split-Hopkinson bar technology. The distance criterion for chip separation was used. Hortig and Svendsen [4] studied the effects of the FE mesh size and orientation on the shear banding and chip formation during HSC. Rhim and Oh [5] found that the localized shear bands and the serrated chips could be predicted by using a rigid plastic FE simulation during a conventional cutting process. Ng et al. [6] developed 2D and 3D FE models to investigate the effect of chip morphology on cutting force, temperature field, stress, and strain distributions in HSC. Umbrello [7] simulated the chip geometries and cutting forces of both conventional cutting and HSC of Ti6Al4V alloy. However, their simulation was unable to mimic serrated chip formation because their chip separation was based on the effective plastic strain criterion and their treatment on the chip–tool interface friction was too simplified, although they used the Johnson–Cook thermal visco-plastic constitutive equation.

The central issues in a proper modeling of a metal cutting process are the description of material's constitutive behavior, determination of chip separation and treatment of chip–tool friction. To date, these key factors have not been dealt well in the FE studies on the serrated chip formation. An HSC process is strongly non-linear and complex, during which the material in a shear zone bears large strain, high strain rate, and significant temperature rise. Hence, material behavior can only be described by a thermo-viscoplastic constitutive model. With respect to the chip separation in HSC, it is necessary to use a criterion of realistic physical meaning so that a simulation result will not depend on cutting conditions. For instance, the commonly used distance criterion, due to its simplicity, is not suitable for HSC because of the ultra-high speed of a tool tip. On the other hand, some chip separation criteria require a predefined parting line which can insert artificial effects on an HSC simulation. Friction at the chip–tool interface will significantly change the chip formation mechanism during HSC. A chip produced during HSC is in a highly stressed zone with high temperature. An effective friction model must be able to accommodate these effects precisely. More importantly, despite the numerous FE simulations in the literature, most have not been verified by corresponding experiments, leaving many open questions, such as the proper selection of simulation conditions (e.g., parameters for material models, damage criterion, and chip–tool friction). As a result, meaningful quantitative comparisons between experiment and simulation for HSC are unavailable.

This paper will combine the Johnson–Cook thermal-viscoplastic constitutive equation, the Johnson–Cook damage criterion for chip separation, and the modified Zorev model for tool–chip friction description to predict the serrated chip formation and cutting force in HSC without artificial assumptions. This approach will remove the major barrier in the current machining investigations using numerical simulations.

2 FE simulation

2.1 Material modeling

Many materials including AISI 1045 steel have been modeled using an elastic–plastic constitutive equation. Under HSC with large strain, high strain rate and high adiabatic temperature rise (over 1,000°C), this conventional constitutive treatment is no longer appropriate. At the present, the flow stress equations for high strain rate deformation can be classified into two groups: empirical constitutive equations such as Johnson–Cook model [8] and microstructure-based equations such as Zerilli–Armstrong [9] and Gao-Zhang models [10]. The Johnson–Cook model is thermo-viscoplastic, depending on strain-rate and temperature, and is suitable for describing the deformation associated with the strain rate over a large range (10^2 to 10^5 s^{-1}) at significant temperature changes caused by plastic deformation. The material parameters of this model can be determined by high strain rate deformation tests and by examining the material deformation in the primary shear zone during HSC processes. Therefore, the Johnson–Cook model will be used in the present study. In this model, the equivalent flow stress $\overline{\sigma}$ is described by

$$\overline{\sigma} = [A + B(\overline{\varepsilon})^n]\left[1 + CLn\left(\frac{\dot{\overline{\varepsilon}}}{\dot{\overline{\varepsilon}}_0}\right)\right]\left[1 - \left(\frac{T - T_0}{T_{\text{melt}} - T_0}\right)^m\right] \tag{1}$$

where $\overline{\varepsilon}$ is the equivalent plastic strain, $\dot{\overline{\varepsilon}}$ plastic strain rate, $\dot{\overline{\varepsilon}}_0$ reference strain rate (1.0 s^{-1}), T_0 room temperature, T_{melt} melting temperature, A initial yield stress (MPa), B hardening modulus, n work-hardening exponent, C coefficient dependent on strain rate (MPa), and m is the thermal softening coefficient. The values of these parameters of AISI 1045 steel are listed in Table 1. Some mechanical and thermo-physical parameters of the steel are given in Table 2.

2.2 Chip separation criterion

As outlined previously, to make a reliable FE simulation, an appropriate chip separation criterion is crucial. The existing

Table 1 Material parameter values for the Johnson–Cook model of AISI 1045 steel [11]

A (MPa)	B (MPa)	n	C	m	$\dot{\overline{\varepsilon}}_0(s^{-1})$	T_{melt} (°C)	T_0 (°C)
553	600	0.234	0.0134	1.0	0.001	1460	20

Table 2 Mechanical and thermophysical parameters of AISI 1045 steel [12]

Density ρ (kg/m^3)	Young's modulus E (GPa)	Poisson's ratio ν	Specific heat C_P (J kg^{-1} °C^{-1})	Heat conductivity λ (W/m°C)
7,800	200	0.3	474	55
Yield strength σ_s (MPa)	Tensile strength σ_b (MPa)	Percentage elongation δ (%)	Reduction of area ψ (%)	Impact toughness A_k (J)
500	700	17	45	80

separation criteria can be divided into two groups, i.e., geometrical and physical. The former is based on simple distance justifications between the tip of a cutting tool and the separation point [13, 14] without any insight of mechanics or material properties. The latter usually integrates some mechanisms of material's failure, such as the failure stress criterion [15–18], effective plastic strain criterion [4, 19, 20] and the strain energy density criterion [21, 22].

There are problems in relation to the application of the existing chip separation criteria as have been pointed out by Zhang [23]. The main issues are as follows. First, using different criteria produce inconsistent results. A good criterion must reflect the mechanical and physical mechanisms of a material subjected to cutting and give rise to reasonable results in every aspect, such as chip geometry, cutting force, temperature distribution and residual stress distribution. Moreover, a sound threshold value of a separation criterion should not vary with cutting conditions when a workpiece material is given, which is unfortunately not the case as Zhang [23] has found out, and none of the existing separation criteria is universal. To use any of them always requires the determination of the special threshold value corresponding to the change of an individual cutting condition. In other words, one cannot use a single threshold of separation for different cutting conditions even when the workpiece material is well defined. Secondly, most of the chip separation criteria are artificial. For example, they need a predefined parting line corresponding to the track of tool tip movement [13–20]. This is unreasonable because in a real machining, the material separation may not take place along a predefined parting line. In addition, the thresholds of critical distance and effective plastic strain have been determined without a sound rule, but based on a trial-and-error process or experimental measurement. Since the results of the FE simulations using these criteria are all different, it is almost impossible to assess their advantages, disadvantages and relationships.

A criterion based on cumulative damage mechanics [24–29] has been proposed. Based on this criterion, a FE can be deleted to realize chip separation when a damage threshold is reached. In this way, there is no need to assume a predefined parting line along a tool movement path, and hence can more realistically reflect the deformation in the tool-material interaction zone. Here, the Johnson–Cook dynamic failure criterion based on the equivalent plastic strain at the element integration points was used. With Abaqus/Explicit software, according to a cumulative damage law

$$D = \sum \left(\frac{\Delta \bar{\varepsilon}}{\bar{\varepsilon}_f} \right) \tag{2}$$

where $\Delta\bar{\varepsilon}$ is the increment of equivalent plastic strain for the element and is updated at every analysis increment and $\bar{\varepsilon}_f$ is the equivalent plastic strain at failure and is expressed as the following equation:

$$\bar{\varepsilon}_f = \left[d_1 + d_2 \exp\left(d_3 \frac{p}{\bar{\sigma}} \right) \right] \left[1 + d_4 Ln\left(\frac{\dot{\bar{\varepsilon}}}{\dot{\bar{\varepsilon}}_0} \right) \right] \left(1 + d_5 \hat{\theta} \right) \tag{3}$$

where, the equivalent plastic strain at failure $\bar{\varepsilon}_f$ is assumed to be dependent on the equivalent plastic strain rate $\dot{\bar{\varepsilon}}$, the ratio $\dot{\bar{\varepsilon}} / \dot{\bar{\varepsilon}}_0$, the ratio of hydrostatic pressure to equivalent stress $p/\bar{\sigma}$ (where p is the pressure stress and $\bar{\sigma}$ is the Mises equivalent stress), and the dimensionless temperature $\hat{\theta} = (T - T_{\text{room}})/(T_{\text{melt}} - T_{\text{room}})$, it also depends on the damage constants d_i (i=1,…5), which are determined experimentally. The damage constants of AISI 1045 steel [26] are presented in Table 3.

The summation in Eq. 2 is performed over all increments in the analysis. The damage parameter D is calculated for each element at each time-step. Once D in an element reaches 1, failure occurs and the element is deleted including the element connectivity and the strain and stress values. ABAQUS/Explicit was used because it enables the application of the damage criterion by the element deletion and remeshing-rezoning technique.

Table 3 Johnson–Cook damage law parameters of AISI 1045 steel [26]

Damage law parameters	AISI-1045 steel
Initial failure strain (d_1)	0.05
Exponential factor (d_2)	4.42
Triaxiality factor (d_3)	−2.73
Strain rate factor (d_4)	0.0018
Temperature factor (d_5)	0.55

2.3 Friction modeling

The friction along the tool–chip interface is an extremely crucial factor. An improper friction description often leads to disagreement between FEM simulations and experimental measurements. Due to the lack of experimental data, Klocke et al. [1], Ng et al. [6], and Umbrello [7] used a simple model such as the Coulomb or the shear friction, ignoring the effect of the normal stress distribution along the chip–tool interface.

A key issue in dealing with the chip–tool interaction in a FE simulation is the treatment of the frictional and normal stress variations on the rake face of a cutting tool. In fact, the normal stress distribution along the tool–chip interface is nonuniform and hence cannot be described well by a single, simple friction model. In general, the normal stress increases monotonically toward the tool edge, leading to different frictional stresses at different locations on the rake face. Under a conventional cutting speed, Zorev [30] proposed two distinct contact regions based on experimental observations, which are the sticking region and the sliding region. The sticking region is defined by an area close to the cutting edge where very high normal stress (σ_n) causes high plastic deformation. In this region, the frictional stress (τ_f) is independent of normal stress and equal to the limit shear stress of the workpiece material ($\tau_{\max}$) [30]. In other words, the rake face of the cutting tool in this region should experience a constant friction determined by $\tau_{\max}$ of the workpiece material. The sliding region locates next to the sticking region till a point where the chip leaves the tool. In this region, the normal stress is relatively small and hence the Coulomb friction law is generally applicable, i.e., the friction there can be calculated by the product of the Coulomb friction coefficient (μ) and the normal stress. It was suggested [6, 31] that Zorev's friction model could be used for HSC, but unfortunately, the friction characteristics in the sticking region was not observed and analyzed.

During HSC, the material at the chip–tool interface can experience microstructural changes, such as the adiabatic shear, phase transformation and even melting. These make the friction mechanisms in the sticking region more complex. Because of this, the shear friction stress may not always be equal to, but highly likely less than the limit shear stress of a workpiece material depending on cutting condition.

In this study, the above mechanism was taken into account. A shear friction factor of $m_f \leq 1$ was introduced to describe the friction in the sticking region. The normal stress at the interface is calculated from the deformation. Whether a contact point is in the sliding or the sticking region depends on the normal stress σ_n at the point, as illustrated in Fig. 1. Mathematically, it can be described by Eq. 4 below:

$$\begin{cases} \tau_f = \mu\sigma_n & if \quad \mu\sigma_n < m_f\tau_{\max} \quad (sliding\ region) \\ \tau_f = m_f\tau_{\max} & if \quad \mu\sigma_n \geq m_f\tau_{\max} \quad (sticking\ region) \end{cases} \tag{4}$$

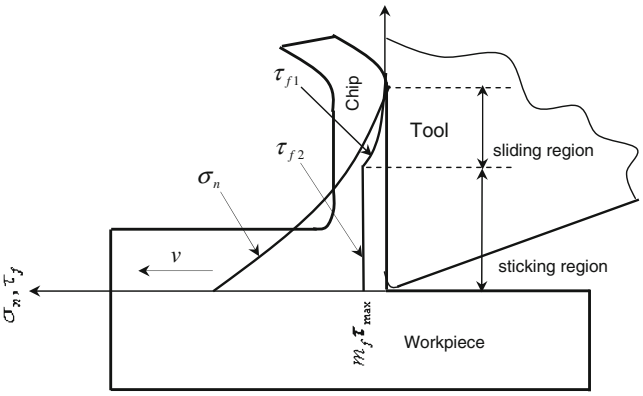

Fig. 1 Curves representing normal and frictional stress distributions on a tool rake face in HSC

Experimentally, it is difficult to obtain accurately the shear friction factor m_f and Coulomb friction coefficient μ. In our simulation, the initial m_f was set as one, and the initial μ was taken as the ratio of the frictional force (F_f) to the normal force (F_n) on the tool rake face [31] which were calculated from the measured force components at a given rake angle α, i.e.,

$$F_{n,\text{estimated}} = \left(F_{c,\text{measured}}\right)\cos\alpha - \left(F_{t,\text{measured}}\right)\sin\alpha \tag{5}$$

$$F_{f,\text{estimated}} = \left(F_{c,\text{measured}}\right)\sin\alpha + \left(F_{t,\text{measured}}\right)\cos\alpha \tag{6}$$

Thus, the initial friction coefficient μ_i was calculated as follows:

$$\mu_i = \frac{F_{f,\text{estimated}}}{F_{n,\text{estimated}}} \tag{7}$$

The final determination of m_f and μ were by iteration on cutting forces by comparing the predicted cutting forces with those experimentally obtained, until their difference were negligible. In this study, $\tau_{\max}$=500 MPa was obtained from experiment [12].

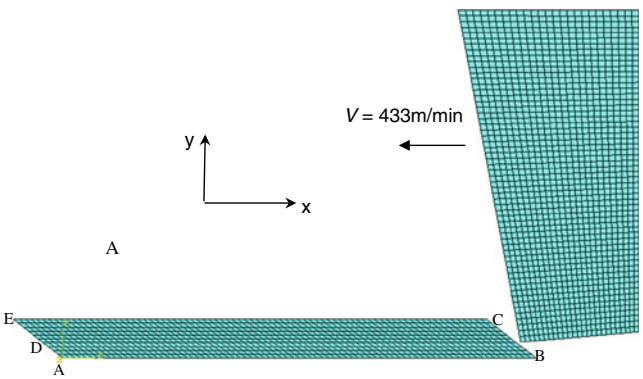

Fig. 2 The FE model of the plane-strain orthogonal cutting

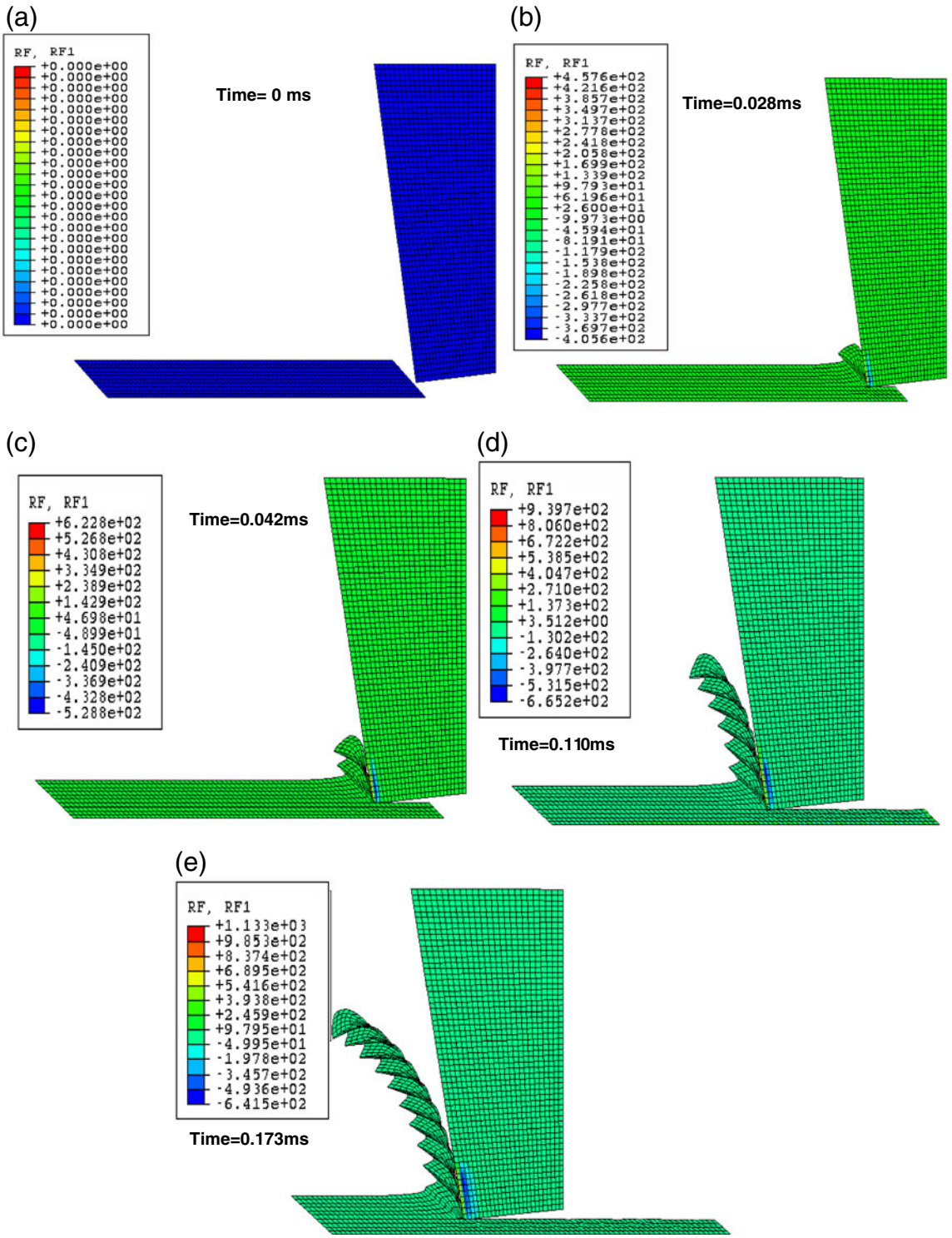

Fig. 3 Whole process of serrated chip formation for rake angle −10° in simulation

2.4 FEM Model

ABAQUS/Explicit was used to construct a plane-strain orthogonal cutting model, whose implicit Lagrangian code offers a very stable remeshing routine. As shown in Fig. 2, the workpiece was discretized by four-noded bilinear elements with reduced integration (CPE4R). To have a better convergence at the final stage of the simulation, the meshes were oriented at an angle of 45° to the cutting plane [7, 25]. To save calculation time, a small workpiece control volume was used (2×0.25 mm), divided by 800 elements of 25×25 μm in dimension. According to the investigations by

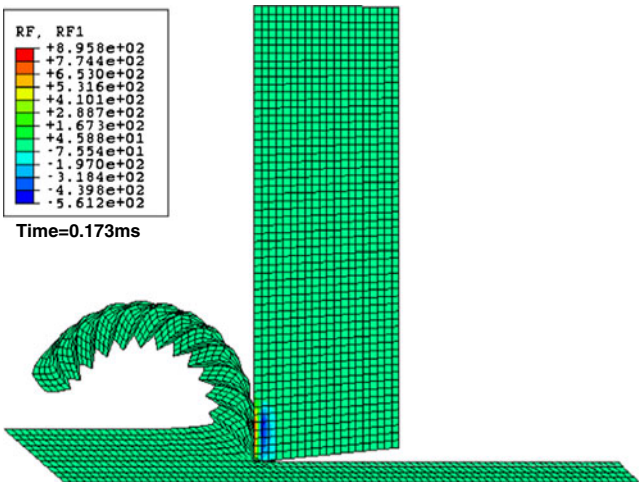

Fig. 4 Morphology of serrated chip for rake angle 0°

Hortig et al. [7] and Mabrouki et al. [25], such control volume and mesh orientation do not influence simulation accuracy of cutting forces and chip geometry. The cutting tool was assumed to be rigidly elastic, divided by 1,450 elements when the rake angle was −10°, 1,160 elements when the angle was 0°, and 870 elements when the angle was 10°. Here, we mainly focused on simulating and predicting the chip geometry and cutting force, which are affected significantly by the tool rake angle, only the rake angle was therefore changed. The cutting conditions used were: cutting speed=433 m/min; cutting thickness=0.15 mm; tool rake angle=−10°, 0°, and 10°; and tool flank angle=5°.

In the simulation, no parting line was predefined, the workpiece edges (EDABC) are rigidly fixed in the space while the cutting tool moving horizontally with a constant velocity v from the right to the left.

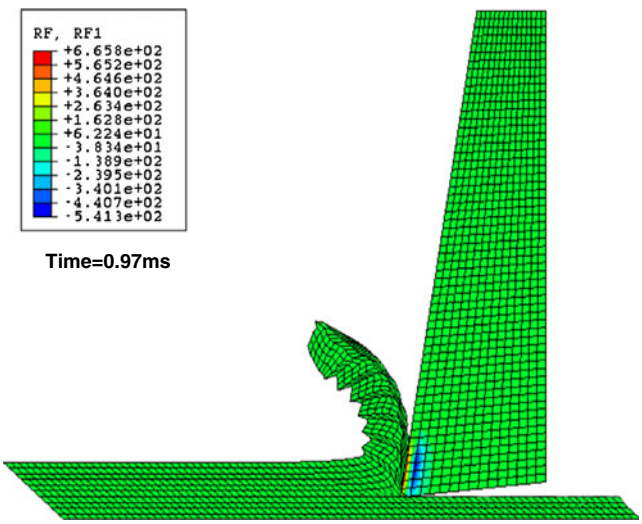

Fig. 5 Morphology of serrated chip for rake angle 10°

Table 4 Friction coefficients and contact length of tool–chip at different rake angles

Rake angle	Friction coefficient		Contact length of tool–chip/mm
	μ_f	μ	
−10°	0.9	0.27	0.3
0°	0.8	0.20	0.2
10°	0.75	0.18	0.175

HSC is a process with large localized deformation, thus the initial mesh was distorted under deformation. The adaptive re-meshing technique in ABAQUS was therefore adopted. In order to take into account the contribution of thermal softening to chip serration, the simulations include the adiabatic heating effects.

3 Experimental verification

The workpiece material was AISI 1045 steel. Ingots of the steel before heat treatment were machined into hollow cylindrical workpieces with the diameter of φ153 mm and thickness of 2.5 mm. The heat treatment process was as follows: heating the workpiece to 850°C in vacuum and maintaining at this temperature for 70 min; then quenching it in salt water, followed by a tempering at 430°C for 5 h. The obtained hardness of a workpiece was HRC35. The cutting tool was a carbide blade, YT15. The HSC was a dry end turning process carried out on a lathe, CA6140. In order to keep the sharpness of the cutting tool noses, the cutting inserts were replaced as required during the experiment. Both the experimental and simulated cutting conditions mentioned above were the same. A 3D piezoelectric turning dynamometer, YDX-III9702, with a response frequency of 2 kHz was used to measure the principal cutting

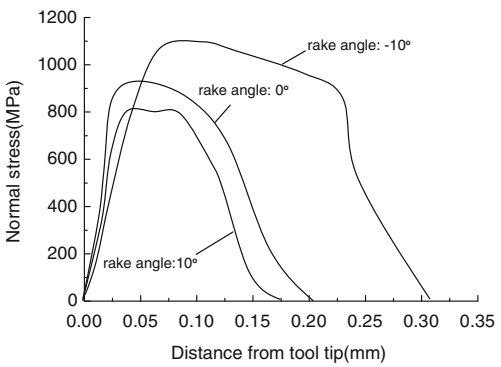

Fig. 6 Calculated normal stress distribution at chip–tool surface at different rake angles

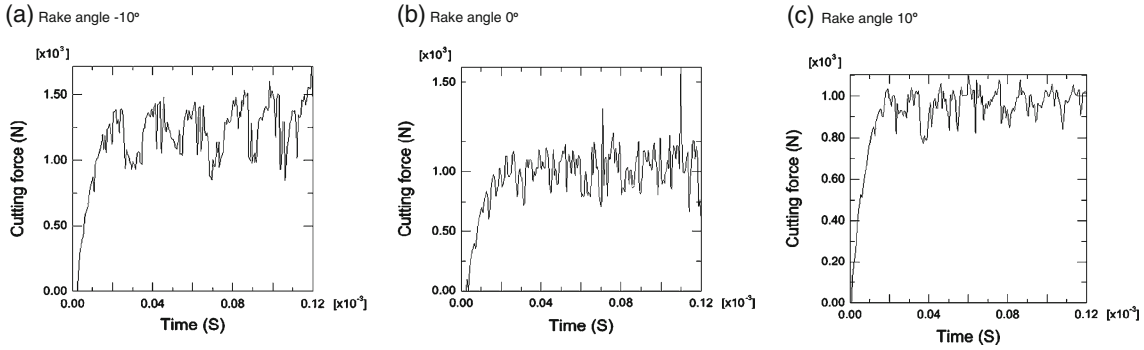

Fig. 7 Curve of principal cutting force F_c at different rake angles

force F_c and the thrust cutting force F_T. The direction of the dynamometer system was defined as follows: X—the main direction of movement and Y—the feed direction. Each set of the measured data were transferred to a computer and analyzed via the dynamometer system software. All experiments were replicated twice under each cutting condition.

To observe and measure the serrated chip geometry, chips obtained were put vertically in the mixing solution of epoxy resin and curing agent. The chip samples were then ground after the solidification of the epoxy, polished and etched using nitric acid alcohol solution to obtain the metallographic surfaces. The chip morphology was observed under a Neuphot-IIOptical Microscope.

4 Results and discussion

4.1 Chip formation

Figure 3 shows the whole process of chip formation and the change of effective stress distribution when the tool rake angle is −10°. Figures 4 and 5 present the chip morphology when the rake angles are 0° and 10°, respectively. The friction coefficients and tool–chip contact length for the three cases of different rake angles, as listed in Table 4, were determined by the iteration method described previously, which shows that the friction coefficients and tool–chip contact length are sensitive to rake angle. As the rake angle decreases, both the friction coefficient and the tool–chip contact length increase. This is because decreasing the rake angle reduces the cutting forces F_c and F_T. According to Eqs. 5, 6, and 7, the calculated normal stress distribution at the chip–tool interface with different rake angles was obtained as shown in Fig. 6. It was found that as the rake angle decreases, the normal stress increases leading to a long and intimate contact between the chip and rake surface yielding higher apparent coefficient of friction. On the other hand, the increment of the frictional force (F_f) is more than that of the normal force (F_n), leading to an increase of the friction coefficient μ in the sliding region. At the same time, the increase of the frictional force in the sticking region results in the advance of shear friction factor μ_f. Furthermore, it is clear that as the friction coefficient increases, the chip curvature becomes smaller and the tool–chip contact zone gets longer. It is worthwhile to note that the remeshing technique applied has successfully arrested the errors from element distortion.

4.2 Cutting force

Figure 7 shows the variation of the principal cutting force with cutting time. We can see that as the tool starts to cut, the cutting force rises sharply, followed by a strong oscillation. This is due to the repeated sawtooth formation caused by the shear deformation localization in the primary shear zone. With the decrease in rake angle, a greater friction coefficient leads to a larger oscillation and higher level of the cutting force. It is worth to note that the simulated oscillation frequency of cutting force F_c and the chip segmentation frequency, as shown in Fig. 8, are consistent,

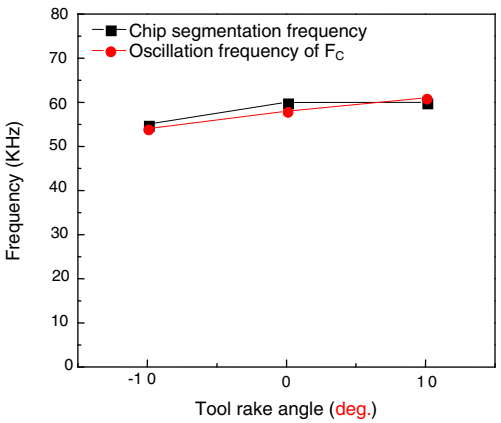

Fig. 8 Oscillation frequency of cutting force F_c and segmentation frequency of the chip

confirming that it was the periodic formation of the sawtooth that had led to the oscillation of the cutting force.

Figure 9 shows the normal and effective stress distribution at the chip–tool surface and in the cutting tool (rake angle=−10°). As can be seen, the compressive stress reaches its maximum at a short distance away from the tool tip. This is consistent with the previous analysis about the chip–tool interface stress. The compressive stress is on the rake tool surface (red color), but tensile stress (blue color) appears in almost the immediate subsurface. (Note that in the figure "+" means "compressive" and "−" means "tensile".) This was because of the large temperature gradient from the rake surface to the subsurface during HSC.

5 Comparison with experiment

5.1 Chip morphology

The predicted and experimentally measured chip morphologies at different rake angles are compared in Fig. 10. Both the experimental and predicted results show that the plastic shear straining in a chip is localized within the shear bands (the primary shear zones), and that the material between the shear bands is only slightly deformed. Generally, sawtooth degree D_s and chip segmentation frequency f_{chip} are used to describe the deformation and geometry of serrated chip in HSC [32], where f_{chip} means the number of sawtooth produced per unit time and D_s is defined by $(H-h)/H$ as shown in Fig. 10a.

Figures 11 and 12 compare the experimental and predicted D_s and f_{chip}, respectively, showing that they are in good agreement. On the other hand, it can be seen that the rake angle has a significant effect on the chip morphology. As the rake angle decreases, D_s increases and f_{chip} decreases. This is because when the rake angle varies from a positive to a negative value, the primary shear zone experiences a stress state of combined compression and shear, which is conducive to the occurrence and development of deformation localization in the primary shear zone [33, 34]. Meanwhile, with increasing the rake angle the compressive stress drops and shear stress becomes dominant, reducing the possibility of further deformation localization. In this case, the sawtooth degree becomes smaller to coordinate the deformation through the whole chip. Hence, the chip segmentation frequency increases. In the metallographic photos of the serrated chips shown in Fig. 10, the adiabatic shear bands are clearly observed, indicating that the adiabatic shear phenomenon occurred could be a root reason of the serrated chip formation.

Here, the same damage parameters d_i (i=1, … 5) were used for all the three cases of different rake angles. An excellent agreement with the experiment was obtained. This means that the parameters determined for the J–C constitutive and those for the damage models in our simulations are precise. It is therefore reasonable to conclude that the application of the J–C damage criterion for chip separation in HSC can avoid the problems in the simulations by other criteria as pointed out by Zhang [23].

5.2 Cutting force

The experimental and the predicted average cutting forces are shown in Figs. 13 and 14, showing once again their good agreement. The results show that the rake angle can influence significantly the cutting forces. As the rake angle decreases, the normal force across the tool–chip interface becomes larger as shown in Fig. 6, which in turn causes a greater friction and cutting force.

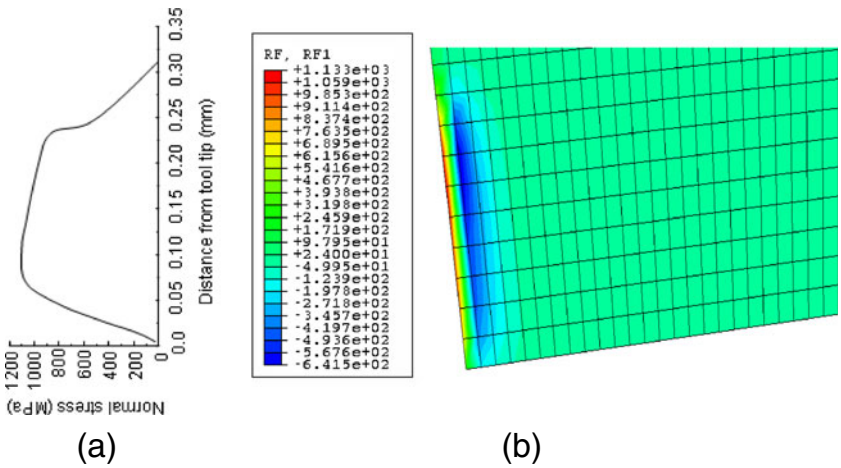

Fig. 9 Effective stress distribution at chip–tool surface and in the cutting tool (rake angle=−10°). **a** calculated normal stress at chip–tool surface; **b** simulated stress distribution at rake tool surface and in tool

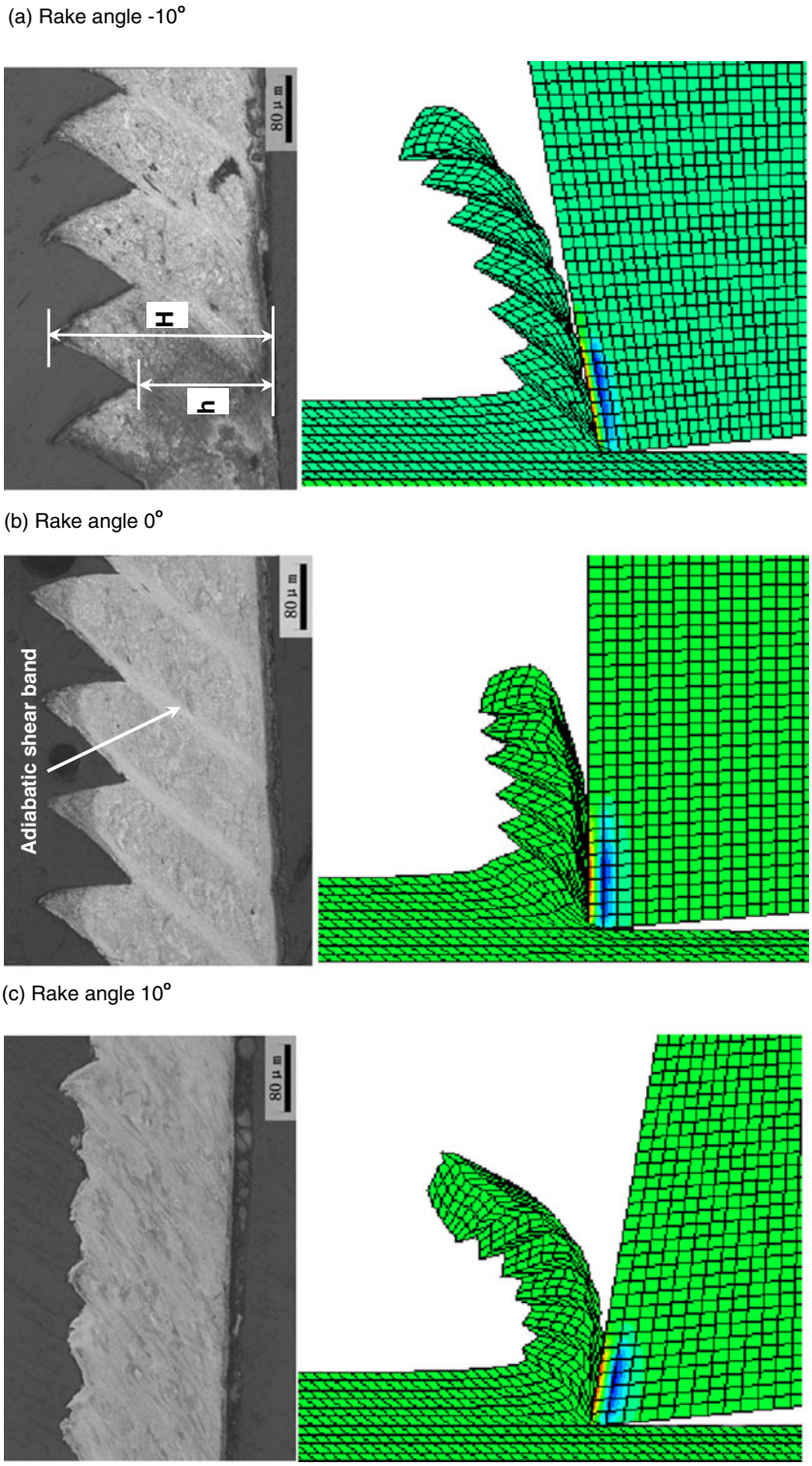

Fig. 10 Comparison between experimental and simulated chip morphology at different rake angles

The above comparison demonstrates that the modified Zorev's friction model used in our study can reasonably reflect the friction nature at the tool–chip interface. This suggests that it is possible to devise a practical procedure for establishing a friction model for the tool–chip contact interface and for calibrating the friction parameters in the modeling, by using a combined experimental-computational approach as we used here.

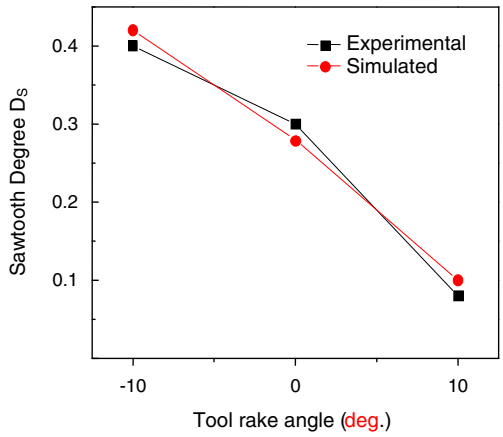

Fig. 11 Comparison between experimental and simulate sawtooth degree under different tool rake angles

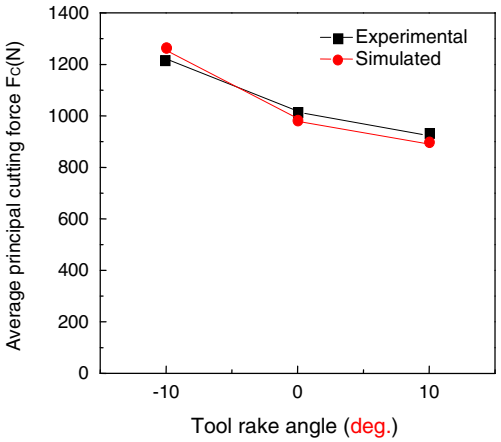

Fig. 13 Comparison between experimental and simulate average principal cutting force under different tool rake angles

6 Conclusions

This paper has carried out both numerical and experimental analyses of serrated chipping during the HSC of AISI 1045 steel. The study has led to the following contributions and conclusions:

1. Using the Johnson–Cook thermal-viscoplastic constitutive equation, the Johnson–Cook damage criterion for chip separation, and the modified Zorev model for tool–chip friction description, the FE method can precisely predict the serrated chip formation and cutting force in HSC without artificial assumptions such as the predetermined parting path and tool–chip separation distance. This has removed the major barrier in the numerical simulation of cutting.
2. For a given workpiece material, the damage parameters can be uniquely determined independent of the cutting conditions. The application of the J–C damage criterion for chip separation in HSC can avoid the problems in the simulations using other criteria.
3. Chip–tool friction can be well described by the modified Zorev model proposed in this paper. The friction is sensitive to the tool rake angle. As the angle increases, both the friction coefficient and the tool–chip contact length decrease. With the decrease in rake angle, a greater friction coefficient leads to a larger oscillation and higher level of the cutting force.
4. The rake angle influences significantly the chip formation and the variation of cutting forces. As the rake angle increases, the chip sawtooth degree and cutting forces decrease but the chip segmentation frequency increases.

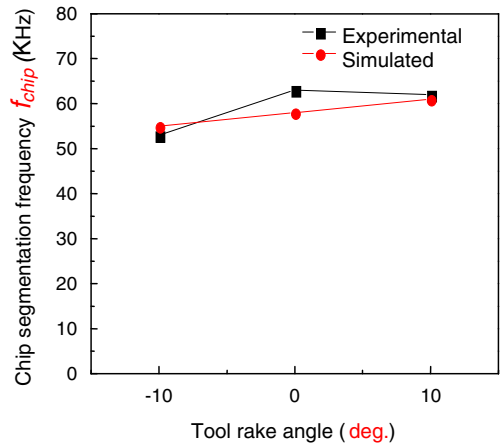

Fig. 12 Comparison between experimental and simulate chip segmentation frequency under different tool rake angles

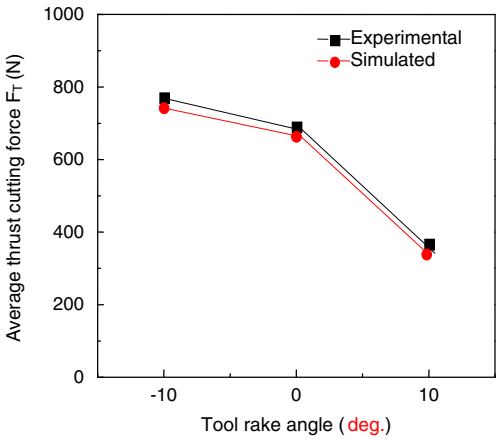

Fig. 14 Comparison between experimental and simulate average thrust cutting force under different tool rake angles

Acknowledgments The authors would like to thank the financial support to this research from both the Chinese Natural Science Fund (no. 50875033) and the Australian Research Council.

References

1. Klocke F, Raedt HW, Hoppe S (2001) 2D-FEM simulation of the orthogonal high speed cutting process. Mach Sci Technol 5 (3):323–340
2. Baker M, Rosier J, Siemers C (2002) A finite element model of high speed metal cutting with adiabatic shearing. Comput Struct 80:495–513
3. Baker M (2006) Finite element simulation of high-speed cutting forces. J Mater Process Technol 176:117–126
4. Hortig C, Svendsen B (2007) Simulation of chip formation during high-speed cutting. J Mater Process Technol 186:66–76
5. Rhim S, Oh S (2006) Prediction of serrated chip formation in metal cutting process with new flow stress model for AISI 1045 steel. J Mater Process Technol 171:417–422
6. Ng EG, EI-Wardany TI, Dumitrescu M, Elbestawi MA (2002) Physics-based simulation of high speed machining. Mach Sci Technol 6:301–329
7. Umbrello D (2008) Finite element simulation of conventional and high speed machining of Ti6Al4V alloy. J Mater Process Technol 196:79–87
8. Johnson GR, Cook WHA (1983) Constitutive model and data for metals subjected to large strain, high strain rates, and high temperature. In: Proceedings of the 7th International Symposium on Ballistics, Hague, the Netherlands, pp 541–547
9. Zerilli FJ, Armstrong RW (1987) Dislocation-mechanics-based constitutive relations for material dynamics calculation. J Appl Phys 5:1816–1825
10. Gao CY, Zhang LC (2010) A constitutive model for dynamic plasticity of FCC metals. Mater Sci Eng A 527:3138–3143
11. Davies MA, Cao Q, Cooks AL (2003) On the measurement and prediction of temperature fields in machining AISI 1045 Steel. CIRP Ann Manuf Technol 52(1):77–80
12. Li GH (2009) Prediction of adiabatic shear in high speed machining based on linear pertubation analysis. Ph.D thesis, Dalian University of Technology, China
13. Komvopoulos K, Erpenbeck AS (1991) Finite element modeling of orthogonal metal cutting. ASME J Eng Ind 113:253–267
14. Lin ZC, Lo SP (1997) Ultra-precision orthogonal cutting simulation for oxygen-free high-conductivity copper. J Mater Process Technol 55:281–291
15. Mamalis AG, Horvath M, Branis AS, Manolakos DE (2001) Finite element simulation of chip formation in orthogonal metal cutting. J Mater Process Technol 110:19–27
16. Huang JM, Black JT (1996) An evaluation of chip separation criteria for the FEM simulation of machining. J Manuf Sci Eng 118:545–554
17. Shet C, Deng X (2003) Residual stresses and strains in orthogonal metal cutting. Int J Mach Tools Manuf 43:573–587
18. Li K, Gao XL, Sutherland JW (2002) Finite element simulation of the orthogonal metal cutting process for qualitative understanding of the effects of crater wear on the chip formation process. J Mater Process Technol 127:309–324
19. Strenkowski JS, Carroll JT (1985) A finite element model of orthogonal metal cutting. ASME J Eng Ind 107:349–354
20. Xie JQ, Bayoumi AE, Zbib HM (1998) FEA modeling and simulation of shear localized chip formation in metal cutting. Int J Mach Tools Manuf 38:1067–1087
21. Lin ZC, Pan WC (1993) Thermoelastic plastic large deformation model for orthogonal cutting with tool flank wear, part I: computational procedures. Int J Mech Sci 35:829–840
22. Lin ZC, Lin YY (2001) A study of oblique cutting for different low cutting speeds. J Mater Process Technol 115:313–325
23. Zhang LC (1999) On the separation criteria in the simulation of orthogonal metal cutting using the finite element method. J Mater Process Technol 89–90:273–278
24. Pantale O, Bacaria JL, Dalverny O, Rakotomalala R, Caperaa S (2004) 2D and 3D numerical models of metal cutting with damage effects. Comput Methods Appl Mech Eng 193:4383–4399
25. Mabrouki T, Rigal JF (2006) A contribution to a qualitative understanding of thermo-mechanical effects during chip formation in hard turning. J Mater Process Technol 176:214–221
26. Vaziri MR, Salimi M, Mashayekhi M (2010) A new calibration method for ductile fracture models as chip separation criteria in machining. Simul Mod Pract Theory 18:1286–1296
27. Cockroft MG, Latham DJ (1968) Ductility and workability of metals. J Inst Met 96:33–39
28. McClintock FA (1968) A criterion for ductile fracture by the growth of holes. J Appl Mech 35:363–371
29. Johnson GR, Cook WH (1985) Fracture characteristics of three metals subjected to various strains, strain rates, temperatures and pressures. Eng Fract Mech 21(1):31–48
30. Zorev NN (1963) Inter-relationship between shear processes occurring along tool face and shear plane in metal cutting. International Research in Production Engineering ASME: International Production Engineering Research Conference, Pittsburgh, pp 42–49
31. Ozel T, Altan T (2000) Determination of workpiece flow stress and friction at the chip–tool contact for high-speed cutting. Int J Mach Tools Manuf 40:133–152
32. Schulz H, Abele E, Sahm A (2001) Material aspects of chip formation in HSC machining. CIPP Ann-Manuf Technol 50 (1):45–48
33. Zhao QT, Wu GQ, Sha W (2010) Deformation of titanium alloy Ti–6Al–4V under dynamic compression. Comput Mater Sci 50 (2):516–526
34. Sun J, Guo YB (2009) Material flow stress and failure in multiscale machining titanium alloy Ti–6Al–4V. Int J Adv Manuf Technol 41 (7–8):651–659